remote sensing

MDPI

Article

Effects of Day/Night Factor on the Detection Performance of FY4A Lightning Mapping Imager in Hainan, China

Hao Sun [1], Jing Yang [1,*], Qilin Zhang [1], Lin Song [2], Haiyang Gao [1], Xiaoqin Jing [1], Guo Lin [3] and Kang Yang [3]

[1] Key Laboratory of Meteorological Disaster, Ministry of Education (KLME), Joint International Research Laboratory of Climate and Environment Change (ILCEC), Collaborative Innovation Center on Forecast and Evaluation of Meteorological Disaster (CIC-FEMD), Key Laboratory for Aerosol-Cloud-Precipitation of China Meteorological Administration, Nanjing University of Information Science and Technology, Nanjing 210044, China; hao.sun@nuist.edu.cn (H.S.); qlzhang@nuist.edu.cn (Q.Z.); gaohy@nuist.edu.cn (H.G.); xiaoqin.jing@nuist.edu.cn (X.J.)

[2] Qingdao Engineering Technology Research Center for Meteorological Disaster Prevention, Qingdao Meteorological Bureau, Qingdao 266000, China; lsq@qtv.com.cn

[3] Department of Atmospheric and Oceanic Sciences, University of Colorado, Boulder, CO 80309, USA; Guo.Lin@colorado.edu (G.L.); Kang.Yang@colorado.edu (K.Y.)

* Correspondence: jing.yang@nuist.edu.cn

Abstract: In this study, the effect of day/night factor on the detection performance of the FY4A lightning mapping imager (*LMI*) is evaluated using the Bayesian theorem, and by comparing it to the measurements made by a ground-based low-frequency magnetic field lightning location system. Both the datasets were collected in the summers of 2019–2020 in Hainan, China. The results show that for the observed summer thunderstorms in Hainan, the daytime detection efficiencies of *LMI* (DE_{LMI}) were 20.41~35.53% lower than the nighttime DE_{LMI}. Compared to other space-based lightning sensors (lightning imaging sensors/optical transient detectors (LIS/OTD) and geostationary lightning mapper (GLM)), the detection performance of *LMI* is more significantly influenced by the day/night factor. The DE_{LMI} rapidly dropped within about four hours after sunrise while it increased before sunset. For the storms that formed at night and lasted for an entire day, the DE_{LMI} remained relatively low during the daytime, even as the thunderstorms intensified. The poor detection performance of *LMI* during daytime is probably because of the sunlight reflection by clouds and atmosphere, which results in larger background radiative energy density (*RED*) than that at night. During night, *LMI* captured the lightning signals well with low *RED* (8.38~10.63 μJ sr^{-1} m^{-2} nm^{-1}). However, during daytime, signals with *RED* less than 77.12 μJ sr^{-1} m^{-2} nm^{-1} were filtered, thus lightning groups could rarely be identified by *LMI*, except those with extremely high *RED*. Due to the limitations of the Bayesian theorem, the obtained *DE* in this study was "relative" *DE* rather than "absolute" *DE*. To obtain the absolute *DE* of *LMI*, the total lightning density is necessary but can hardly be measured. Nonetheless, the results shown here clearly indicate the strong impact of day/night factor on the detection performance of *LMI*, and can be used to improve the design and post-processing method of *LMI*.

Keywords: FY4A lightning mapping imager; low-frequency magnetic field lightning location system; detection efficiency; Bayesian theorem; day/night factors

Citation: Sun, H.; Yang, J.; Zhang, Q.; Song, L.; Gao, H.; Jing, X.; Lin, G.; Yang, K. Effects of Day/Night Factor on the Detection Performance of FY4A Lightning Mapping Imager in Hainan, China. *Remote Sens.* **2021**, *13*, 2200. https://doi.org/10.3390/rs13112200

Academic Editor: Noam Levin

Received: 5 May 2021
Accepted: 2 June 2021
Published: 4 June 2021

1. Introduction

Lightning produces electromagnetic waves, induces electrostatic field, and creates optical and acoustic signals. Spatial and temporal information and discharge parameters of lightning can be obtained by detecting these various signals. In the 1980s, Wolfe and Nagler proposed an imager that utilized spatial optics to receive the optical signals transmit to the cloud top during lightning discharges [1]. Thomason and Krider used a Monte Carlo method to simulate and analyze the transport of 0.45 μm and 0.87 μm photons produced

by transient light sources, such as lightning, within different clouds and in different source locations [2]. Thereafter, Christian et al. implemented an optical pulse sensor to a U2 aircraft and found that the optical radiation intensity of lightning was the strongest at the near-infrared absorption spectral line of neutral oxygen atoms at 777.4 nm, thereby discovering the primary detection band for lightning mapping imagers used on satellites [3,4].

Subsequently, several sensors (e.g., optical transient detectors (OTD) and lightning imaging sensors (LIS)) were mounted on low-orbit satellites to detect lightning activities. Many researchers have cross-analyzed the data of satellite- and ground-based lightning location system (LLS) to determine the detection performance of the lightning sensors [5–8]. Thomas et al. cross-analyzed three-dimensional lightning data obtained by lightning mapping array and LIS data collected in Oklahoma, USA, and found that the two datasets had excellent spatial and temporal correlations. Intra-cloud discharges were readily detected by LIS as soon as they extended into the upper part of the storm, while cloud-to-ground discharges that were confined to mid- and lower-altitudes were less well detected than intra-cloud discharges [5]. Boccippio et al. used laboratory calibration and the observed background radiance data to determine the effective sensitivities of OTD and LIS, focusing on the diurnal variability. They found the minimum signal-to-noise ratios of LIS and OTD occur from 08:00 to 16:00 local time. The flash detection efficiency (*DE*) was 93 $\pm$ 4% and 73 $\pm$ 11% for LIS at night and noon; 56 $\pm$ 7% and 44 $\pm$ 9% for OTD at night and noon, corresponding to a 12~20% diurnal variability [6]. Thompson et al. cross-analyzed the datasets from LIS, the ground-based World Wide Lightning Location Network (WWLLN) and the Earth Networks Total Lightning Network (ENTLN). They defined a value called coupled percentage (*CP*), which is the ratio of the total stroke number detected by WWLLN (ENTLN) and LIS to the number detected by LIS, and found the total *CP* of ENTLN data was 17.5% higher than that of the WWLLN data, the *CP* of the ENTLN data was the highest in the southeast regions of the North American continent, and the *CP*s for both datasets were higher in winter compared to summer [7]. Bitzer et al. used Bayesian theory to analyze the lightning activity detected in the North American continent in 2013 and found that the *DE* of the LIS was 80.1%, and that of the ENTLN was 40.1% [8].

In order to enable the continuous monitoring of lightning from space, lightning sensors were designed to work on geostationary satellites. The two geostationary orbit lightning sensors currently in operation are the geostationary lightning mapper (GLM) mounted on GOES (geostationary operational environmental satellite)-16 and -17 [9–11] and the lightning mapping imager (*LMI*) mounted on FY4A (FengYun 4A meteorological satellite) [12–14]. The data detected by GLM had been analyzed and evaluated in recent years [11,15–19]. Rudlosky et al. used the initial 9 months GLM data to analyze the diurnal variability of lightning activities over Lake Maracaibo, the land areas surrounding Lake Maracaibo and the central United States. They found the GLM flash area and duration follow similar diurnal trends in the 3 areas, and larger flashes with a nocturnal maximum in both flash area and duration [11]. Peterson et al. applied a lightning reclustered technique to the 2018 GLM data and produced statistics describing the characteristics and frequencies of the reclustered GLM flashes in the American continent. They found the flash rate of the American continent has distinct diurnal variations, the flash rate peaks at around 20:00 UTC [15]. Marchand et al. cross-analyzed the GLM data and ENTLN data of the United States collected in 2017 and 2018. Their analysis suggested that the GLM *DE* is affected by various factors including the different fields of view, lightning type, peak current of flashes and solar zenith angle. Due to the effect of solar zenith angle, the mean flash area and mean flash energy were both greater during the night than the day. The GLM *DE* over the Northern Plains ranged from 43% to 72% while *DE* over the Southeast ranged from 74% to 91% as the solar zenith angle changed [16]. Zhang made an inter-comparison of multiple observations of lightning, and found that compared with LIS data with finer resolution, GLM had a lower efficiency to detect short and small flash because more than half of the light sources were relatively smaller than a GLM pixel size. The short flashes also did not have enough time to propagate and develop large enough to be detected

by GLM [17]. In addition, the *DE* of GLM had also been reported, the mean daily flash *DE* was 73.8%, and detection was the highest during nighttime. Regardless of the storm type, 20~40% small and short-duration flashes and more than 95% large and long-duration flashes could be detected by GLM [18]. Rutledge et al. evaluated GLM *DE* for convective storms characterized by anomalous charge structures and found the GLM *DE* vary with the geometric size of the flash and with cloud water path [19].

The *LMI* equipped on the FY4A geostationary meteorological satellite is the second geostationary lightning detection sensor worldwide following the GLM. It enables the continuous monitoring of lightning activity in East Asia and provides lightning products. In recent years, there have been some studies on *LMI*. These studies showed that the spatial distributions of lightning events measured by *LMI* are generally consistent with ground-based lightning location systems (e.g., Global Lightning Dataset, Lightning Location Information System of Hong Kong Observatory, the Advanced Time of Arrival and Direction system lightning observation network and the WWLLN data) and LIS data [14,20,21]. For example, Hui et al. analyzed the *LMI* performance for a concentrated lightning outbreak over Northeastern India in the pre-monsoon season and over Southeastern China in the monsoon season, and they found the *LMI* measurements were consistent with LIS and WWLLN observations [20]. However, some other studies showed that *LMI* may have large uncertainties for a large angle of views, such as the measurement over the Tibetan Plateau [21]. Although *LMI* has been launched for several years, the data have not been widely used in various studies. This is because the quality of *LMI* data is still not well understood. For the effects of day/night factors on satellite-based lightning sensor performance, there have been many studies on GLM and LIS. However, *LMI* is different from GLM and LIS in both hardware design and post-processing methods, and applying the previous results directly to *LMI* is not appropriate. It is necessary to investigate the detection performance of the *LMI* and the factors influencing its detection efficiency, but the related studies are very limited.

In this study, we evaluated the effect of day/night factor on the detection performance of FY4A-*LMI* by using the Bayesian theorem, and by comparing it to the measurements made by a ground-based low-frequency magnetic field lightning location system. A detailed case study of a summer thunderstorm was undertaken, and the results of 26 different cases that occurred in the summers of 2019~2020 in Hainan, China, were analyzed. To the best of our knowledge, this is the first study that evaluates the day/night effect on the detection performance of FY4A-*LMI* in detail. The findings of this study serve as a reference for optimizing lightning algorithms in future satellite-based lightning detection equipment.

2. Datasets

In this study, the diurnal effect on the *LMI* detection performance is evaluated, and compared to a ground-based lightning location system. Details of the design and retrieval methods of the two systems are described in this section. In addition, the cloud top temperature retrieved from Advanced Geosynchronous Radiation Imager (AGRI) observation is delineated as it will be used to display the development of thunderstorms.

2.1. Low-Frequency H-Field Lightning Location System (LLS) (L3D) Data

We established a ground-based low-frequency H-field LLS in Hainan Island, China, in the summer of 2019 (Figure 1a). The Hainan Island, located in the southernmost part of China has a tropical monsoon climate, with an average annual temperature of 22~26 °C and an annual relative humidity greater than 80%. The island has mountainous west and is mainly plains in the east. Most of mountains are 500~800 m above sea level. The annual rainfall over Hainan is approximately 1639 mm. The rainy season lasts from May to September, and accounts for 70~90% of the total annual rainfall. Most of the precipitation events are generated due to the fronts systems, tropical cyclones and typhoons. The thermodynamic effect of terrain and sea-land breeze also have important impacts on the formation of convective clouds [22]. The frequent occurrence of summer convections over

Hainan provides a good opportunity to study the characteristics of thunderstorms and lightning. In this study, we chose the area of 107.2°E~112.6°E longitude and 16.4°N~21.6°N latitude as the research region in this paper (red box in Figure 1b). The reason to select this region is detailed in Section 3.1.

The system comprised seven monitoring substations, forming a lightning detection network. At each substation, two orthogonal low-frequency H-field antennas with a frequency band of 1~300 kHz, a high-speed data collection system, and a high-precision GPS (global position system) clock were installed. The sampling rate was 1 MHz and the dynamic range was ±10 V. For the frequency band of 1~100 kHz, the measured voltage is proportional to the rate of change in the magnetic induction (dB/dt). In contrast, for frequencies at 100~300 kHz, the measured voltage is proportional to the magnetic induction (B). The purpose of this design was to obtain more information of dB/dt in the signals and to identify the rapidly changing pulses. A trigger sampling method was adopted for the detection system to synchronously and continuously collect, record, and transmit the waveform data in real time. To compensate for environmental differences, the trigger threshold was set as 110~120% of the environmental noise. A pre-trigger time period of 300 μs was used so the data before the trigger moment was also recorded. Once the synchronous waveform signals from a lightning were collected by the substations, a cross-correction technique [23] was employed to find the matched waveform data of each lightning activity recorded by different substations. For instance, Figure 2a,b shows the pulse waveforms of a single lightning detected by seven monitoring substations in Hainan, which occurred at 12:47 UTC + 8 on 22 August 2019. Subsequently, the time-of-arrival (TOA) method [23–25] was adopted to calculate the occurrence time and location (Figure 2c,d) of the radiation pulse source.

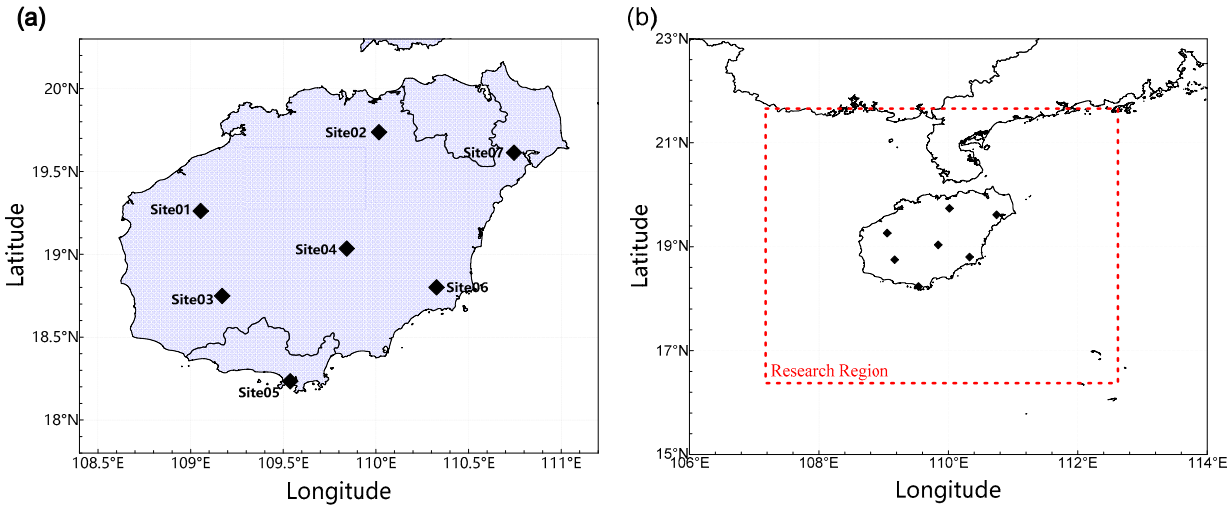

Figure 1. (**a**) Location of the low-frequency H-field lightning location system (LLS) in Hainan, China. The system is comprised of seven monitoring substations (represented as black diamonds) that utilized low-frequency H-field antennas, a high-speed data collection system, and a high-precision GPS (global position system) clock. The red box in (**b**) is the research region of the paper.

The development of the ground-based low-frequency H-field LLS began in 2017 and was first used in 2018 in Nanjing, China. Monte Carlo theory simulation and other synchronized remote sensing data were used to evaluate the performance of this LLS [26]. By using a finite difference time domain (FDTD) technique, the spatial location error in the detection network was evaluated to be less than 150 m. The locations of pulses showed great consistency with the region with cold cloud-top temperature and intense radar echo. In addition, the LLS locations were compared with an independent lightning detection system in Nanjing [27], and the results showed that there was little difference in the locations of the two LLSs, with 80% of the location point distance less than 1 km. In this paper, we

used the same LLS in Hainan, the installation and test of all substations were completed before August 2019, and the field measurement started on 1 August. The datasets serve as a reference to evaluate the FY4A-*LMI* data, and to study the characteristics of lightning activity in Hainan. In the summers of 2019 and 2020, the data from 26 thunderstorm cases were recorded. All the data collected from these cases were used for analysis. Among the 26 cases, 21 produced lightning activity in the daytime period (08:00~16:00 UTC + 8) and 20 produced lightning activity in the night period (20:00~04:00 UTC + 8).

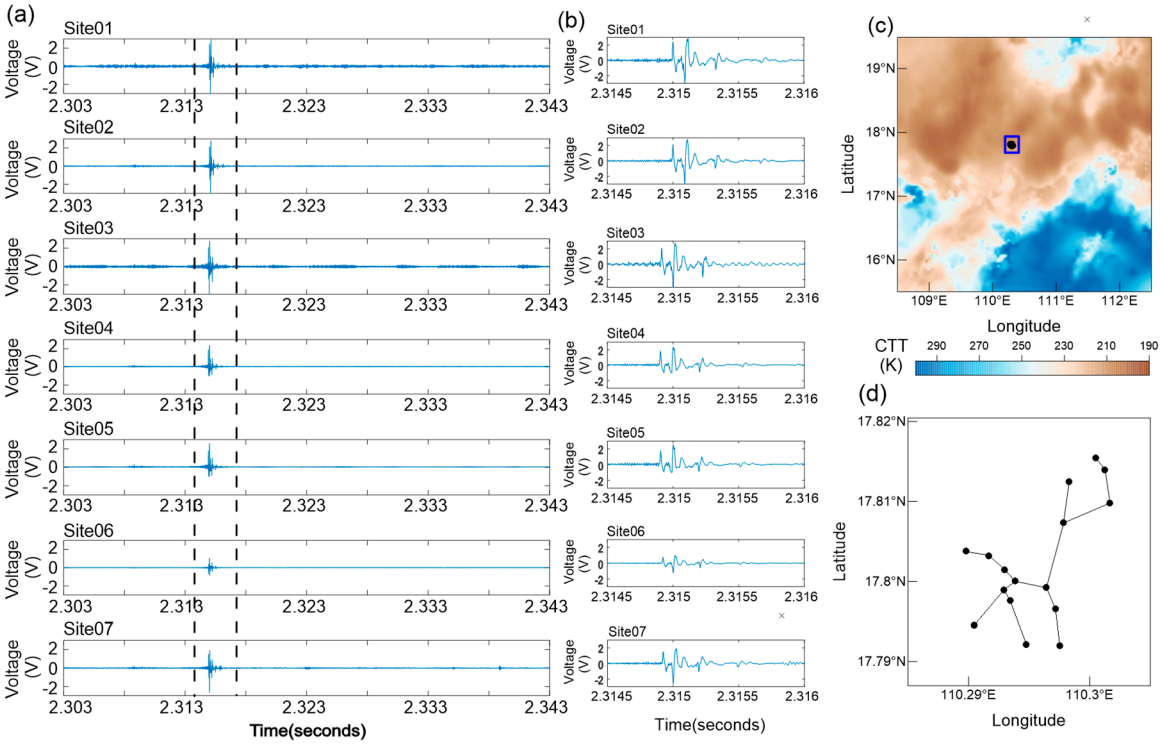

Figure 2. (**a**) The pulse waveforms of a single lightning detected by seven monitoring substations in Hainan, discharge occurred at 12:47 UTC + 8 on 22 August 2019; (**b**) is the part of (**a**) between the two dotted lines; (**c**) the locations of the lightning and the cloud top temperature (unit: K) at the same time; (**d**) is the channel structure of lightning in the blue box of (**c**), ● represents the locations calculated by time-of-arrival (TOA).

2.2. FY4A Lightning Mapping Imager (LMI) Group (LMIG) Data

The *LMI* is the first space-based lightning detection sensor developed in China, and is currently mounted on the geostationary meteorological satellite FY4A [12–14,20,21], positioned at 104.7°E above the equator and approximately 36,000 km from the Earth's surface. It uses ultra-narrow bandpass filters with a central wavelength of 777.4 nm and a bandwidth of 1 nm, and has a resolution of 7.8 km at nadir and increasing to 24.2 km at the edge of its full-disk view. The sensor comprises two 400-by-600 charge-coupled devices (CCDs) capable of collecting the optical radiation energy of lightning at a pixel integration of 2 ms.

When a signal is detected by CCDs, a multi-frame average background noise estimation is used by the real-time event processor (RTEP) to filter the background noise. The filter threshold is determined from the average background noise of several frames before the current frame. Similar to GLM, during the daytime, the reflection of sunlight by clouds and atmosphere creates a larger background noise [28]. Therefore, there is a dynamic filter threshold of *LMI* diurnally. After filtering, the possible "events" from lightning are extracted, and the data are sent to the ground station in real time. The data are then calibrated, the false lightning signals and cluster are removed, and the useful lightning

signals are post-processed to generate the product datasets, which contains the time of occurrence, location, energy density, etc. of events and groups.

In this paper, we use the lightning group dataset, which is generated using the same clustering method as the LIS/OTD [29–31]. In this method, lightning events that occurred within the same time frame and in adjacent pixels were clustered to a group. The *LMIG* dataset is well defined and can be compared with ground-based lightning detection data.

2.3. FY4A Cloud-Top Temperature (CTT) Data

The AGRI that the FY4A is equipped with is comprised of 14 channels that covers a frequency bandwidth from visible through the infrared spectrum (0.45~13.8 μm) [32,33]. Cloud top temperature (CTT), which is often used to investigate the development of convective clouds, is one of the level-2 products of AGRI, and is used in this study to describe the formation, growing and dissipation of thunderstorms [34]. The AGRI adopts a detection approach that alternates between full-disk and regional coverage. The temporal resolution of the full-disk scanning mode is 15 min, and that of the regional scanning mode is approximately 4 min. The spatial resolution for both modes is 4 km at nadir. AGRI uses the geostationary orbit normal projection and the geographic coordinates are calculated using the WGS84 reference ellipsoid, therefore, the column and line numbers of the detection data can be converted into geographic latitude and longitude values. The observation scope of AGRI is 70°E~140°E longitude and 15°N~55°N latitude.

3. Analysis Method

3.1. Selection of Research Region

L3D is a lightning detection network composed of seven monitoring substations in Hainan. In theory, the *DE* is the highest within the detection network, and decreases with distance along the radial direction. Therefore, the selected research region should not be too large, otherwise the average *DE* of *L3D* would be underestimated. A sensitivity test is used to determine the optimal research region, in order to ensure that the *DE* of *L3D* does not have a great decrease near the edge of the region. The method is as follows:

Defining the pulse number detected by *L3D* as N_{L3D}, and the number of groups detected by *LMI* is N_{LMI}, the ratio between them is:

$$R = \frac{N_{L3D}}{N_{LMI}} \quad (1)$$

The optimal research region can be determined by gradually increasing the area of research region and calculating the corresponding N_{L3D}/N_{LMI} ratio. Here, 109.0°E~110.8°E and 18.2°N~19.8°N was set as the initial region, and it was enlarged gradually with an interval (Δd) of 0.2°. All the 26 thunderstorm cases were used in the sensitivity test. The results were shown in Figure 3. The daytime and nighttime N_{L3D}/N_{LMI} are shown in Figure 3a,b, respectively. To make the results clearer, the N_{L3D}/N_{LMI} are normalized (Figure 3c,d). The black bold lines are the average N_{L3D}/N_{LMI} and normalized N_{L3D}/N_{LMI}. As seen from the figure, the N_{L3D}/N_{LMI} decreased distinctly when the research region was 9 Δd larger than the initial area, indicating that the DE_{L3D} sharply decrease when range exceeds this threshold. Therefore, the region 107.2°E~112.6°E and 16.4°N~21.6°N (red box in Figure 1b) is used as the research region of this paper. According to the geographic coordinates calculated by the WGS84 reference ellipsoid, the sensitivity of the *LMI* pixel was approximately 12.4 km over Hainan Island. Within the range of 300 km surrounding Hainan Island, the max change of observation degree was about 0.68°, and the pixel variation (which affects the DE_{LMI} in space) was less than 1 km. Thus, the impacts of the variation of pixel size and angles of view on DE_{LMI} were expected to be small within such as small area, and will be demonstrated later in Section 4.2.

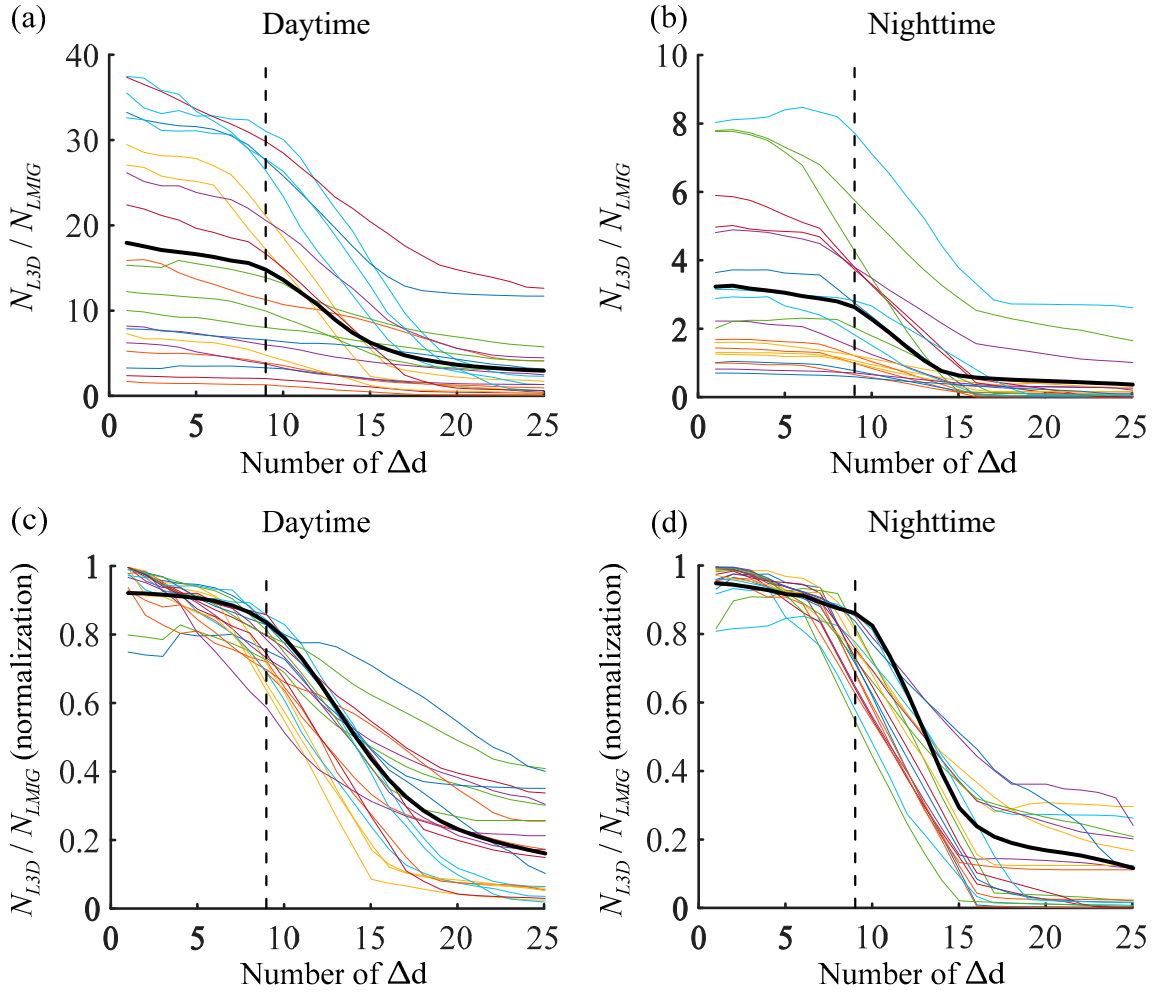

Figure 3. (**a**,**b**) daytime and nighttime N_{L3D}/N_{LMI}, and (**c**,**d**) normalized N_{L3D}/N_{LMI} as the research region enlarged by 0.2° intervals (Δd) from the initial 109.0°E~110.8°E and 18.2°N~19.8°N region. The colored lines represent for different cases, the black bold lines represent for the averages.

3.2. Calculation of Detection Efficiency (DE) Using Bayesian Theorem

The absolute *DE* of LLS can be determined using:

$$P(A) = \frac{N_A}{N} \tag{2}$$

where, N is the total number of lightning discharges and N_A is the number of discharges detected by an LLS. However, the true N is not known. In previous works, it was usually assumed that a standard LLS can detect all lightning discharges (or an absolute *DE* is assumed) to evaluate the *DE* of another LLS. This is not true since different LLSs have their own disadvantages, and no LLS can detect all lighting discharges (i.e., the detection efficiency is not exactly 100%). Strictly speaking, the *DE* calculated from some previous studies were actually relative *DE* rather than absolute *DE*. In order to make the result more scientifically reasonable, the Bayesian theorem [8] is used to evaluate and compare the *DE* of the two LLSs in this paper. According to the Bayesian theorem, the relationship between the conditional probability (relative *DE*) and absolute probability (absolute *DE*) can be found:

$$P(B|A) = \frac{P(A|B)P(B)}{P(A)} \tag{3}$$

where, $P(A)$ and $P(B)$ is the absolute *DE* of two different LLSs, hereafter LLS_A and LLS_B. $P(B \mid A)$ is the conditional probability of LLS_B to detect a discharge which is readily detected by LLS_A, and similarly for $P(A \mid B)$.

The probability of detecting a lightning discharge by either of the LLSs is calculated using the additive law of probability:

$$P(A \cup B) = P(A) + P(B) - P(A \cap B) \tag{4}$$

where $P(A \cup B)$ is the probability of detecting a discharge by either LLS, and $P(A \cap B)$ is the probability of detecting a discharge by both LLSs.

$P(A \cap B)$ is given by the multiplicative law:

$$P(A \cap B) = P(A|B)P(B) \tag{5}$$

$P(A \cup B)$ can be obtained by combining Equations (4) and (5),

$$P(A \cup B) = P(A) + P(B) - P(A|B)P(B) \tag{6}$$

and leads to

$$P(A \cup B) = P(A)\{1 + \frac{P(B)}{P(A)}[1 - P(A|B)]\} \tag{7}$$

Applying Equation (3) to Equation (7), we have,

$$P(A \cup B) = P(A)\{1 + P(B|A)[\frac{1}{P(A|B)} - 1]\} \tag{8}$$

Similarly, we have,

$$P(A \cup B) = P(B)\{1 + P(A|B)[\frac{1}{P(B|A)} - 1]\} \tag{9}$$

Thus, the *DE* of the two LLSs can be calculated,

$$DE_A = P(A) = \frac{P(A \cup B)}{1 + P(B|A)[\frac{1}{P(A|B)} - 1]} \tag{10}$$

$$DE_B = P(B) = \frac{P(A \cup B)}{1 + P(A|B)[\frac{1}{P(B|A)} - 1]} \tag{11}$$

Since there is no reference LLS that has a *DE* of 100%, we cannot know the value of $P(A \cup B)$, so it assumed that by the combination of the two LLSs, all the lightning events can be detected, i.e., $P(A \cup B) = 1$. This is not always true, especially in the daytime, and may lead to an overestimation of the *DE*, which we will discuss in detail later in Section 5. Therefore, the *DE* we obtain is still not the true absolute *DE*, and this limitation needs to be kept in mind in the following analysis. However, compared to the *DE* obtained by assuming one of the LLSs is the ground truth, the *DE* determined by Bayesian theorem is more scientifically reliable, and allow us to have a more robust analysis of the effects of day/night factor on the detection performance of *LMI*.

3.3. Calculation of the Conditional Probability

The $P(B \mid A)$ and $P(A \mid B)$, which indicate the conditional probability of LLS_B and LLS_A, are required for calculating the *DE* of the two LLSs in Bayesian theorem. Therefore, it is necessary to find the two LLSs' matching conditions.

L3D and *LMI* use completely different principles in detecting the lightning discharges. *L3D* captures the VLF/LF (very low frequency/low frequency) band electromagnetic signal emitted by lightning discharges using multiple substations and determined the occurrence time and location by TOA method. *LMI* obtained the data by receiving the light radiation

signal transmitted to the cloud top during lightning discharges. Due to the scattering effect of hydrometeor particles in thunderstorms, and the time delay of *LMI* detection in terms of the propagation of radiation from the source to *LMI*, there might be temporal differences between the results of *LMI* and *L3D*. In addition, the location of *LMIG* data is a weighted location determined by the radiation intensities and distances of events (they were also affected by the type and concentration of hydrometeors, and the distance from the discharge locations to cloud tops), rather than the locations of discharges. Therefore, there is also spatial differences between the locations obtained by *LMI* and *L3D*. Due to these differences, it is necessary to determine a reasonable time window and spatial grid for the matching between the two datasets, i.e., for any lightning event observed by one of the LLS, we search for the corresponding lightning events observed by the other LLS within a given time-space constraint to calculate the conditional probability.

Here, we conducted a sensitivity test [7] to determine the time-space constraint. It is preferred that the time frame and spatial grid is as small as possible, otherwise different lightning events may be mismatched, leading to an overestimation of the conditional probability. However, the time frame and spatial grid should be at least larger than the possible systematic temporal and spatial differences between the two datasets. Figure 4 shows the results of P (*LMI* | *L3D*) and P (*L3D* | *LMI*) for different time-space constraints. As seen from the figure, the conditional probability increases rapidly as the time frame (Figure 4a,b) and spatial grid (Figure 4c,d) increases to 2 s and $0.3^\circ \times 0.3^\circ$, and continues to increase steadily. The high sensitivity of P (*LMI* | *L3D*) and P (*L3D* | *LMI*) to the time-space constraint for time frame <2 s and spatial grid $<0.3^\circ \times 0.3^\circ$ reveals the possible systematic differences between the two LLSs. Therefore, we use a time-space constraint of 2 s and $0.3^\circ \times 0.3^\circ$ to calculate P (*LMI* | *L3D*) and P (*L3D* | *LMI*). We find the criteria determined in this paper is similar to that obtained by Hui et al. [20] who analyzed the LMIG and WWLLN data (2.1 s, 40 km). Compared with the time-space constraint used for the low-orbit space-based LLS and ground-based LLS made by Thompson et al. [7] and Bitzer et al. [8] (0.4 s, 0.15° and 0.01 s, 20 km), the time frame of geostationary orbit space-based LLS is longer. In fact, we tried to use the time-space constraint (0.52 s, 0.15°, considered the time difference for lightning radiance transmit from thunderstorms to low orbit and to geostationary orbit) used by Thompson et al. [7], the mean P (*LMI* | *L3D*) and P (*L3D* | *LMI*) are only 5.78% and 10.72%, indicating that time-space constraints made by low orbit LLS is not suitable for *LMI*.

It is common that within the defined time-space constraint, multiple *L3D* pulses may be matched to an *LMIG*, or multiple *LMIG*s may be matched to a *L3D* pulse. To address this issue, we follow the method introduced in Bitzer et al. [8]. An *LMIG* can be matched only to a single *L3D* pulse, as each pulse should produce independent optical emission. While a *L3D* pulse is allowed to be associated with every *LMIG* that satisfies the time-space constraint, this is because the pulse from a single return stroke can be split across frames, resulting in more than one group, yet one physical discharge. Given that the 2 s time constraint is longer than the typical duration of a discharge, this methodology tends to overestimate P (*L3D* | *LMI*), and this uncertainty will be discussed later in Section 5.

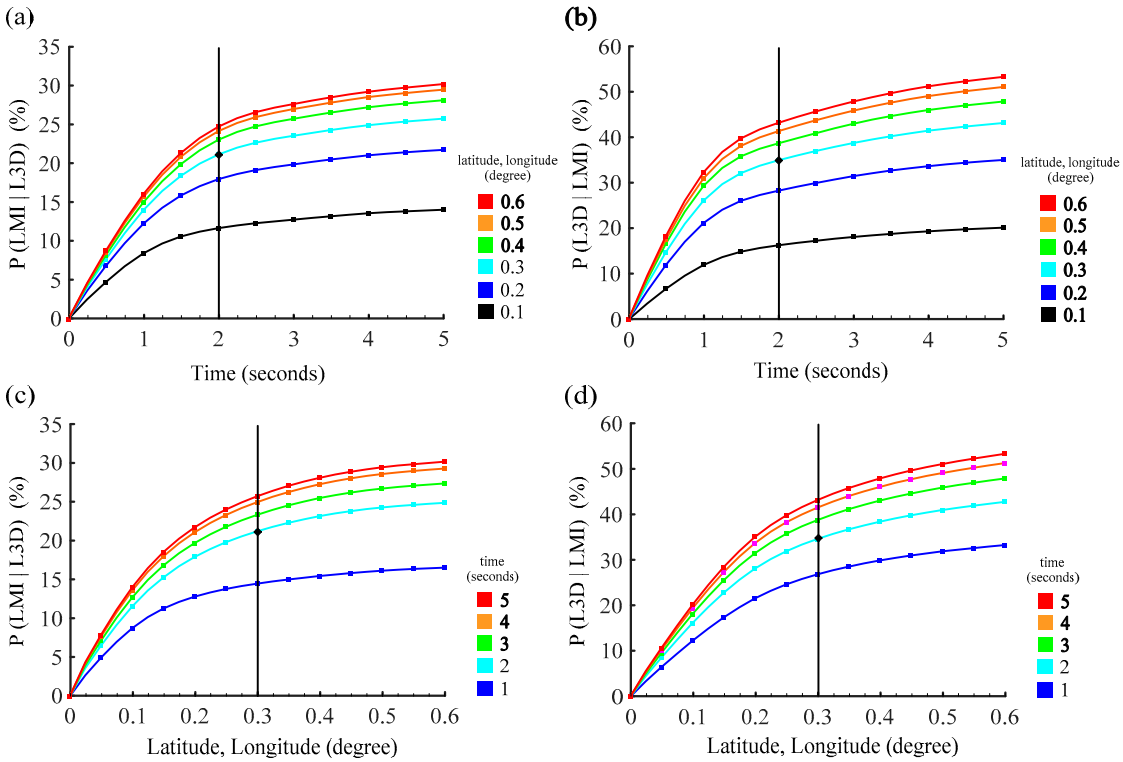

Figure 4. (**a**) The *P* (*LMI* | *L3D*) and (**b**) *P* (*L3D* | *LMI*) as a function of time frame for different latitude and longitude constraints (color lines). The vertical black line indicates the selected time constraint. (**c**,**d**) *P* (*LMI* | *L3D*) and (**b**) *P* (*L3D* | *LMI*) as a function of space constrain for different time frames. The vertical black line indicates the selected latitude and longitude constraint.

4. Results

4.1. A Case Study (Storm0821)

Storm0821 formed at 23:15 on 21 August 2019 and dissipated at 22:45 on 22 August 2019. In this study, time is expressed in UTC + 8, approximate to Hainan local time. The near-surface ambient temperature was approximately 29 °C at 23:00 21 August and the sea-level pressure was approximately 1015 hPa. The wind field derived from NCEP reanalysis data indicated southwesterly low-level wind, bringing warm moist air to the area surrounding Hainan. Low-level potential instability was observed according to the sounding data, and the convective available potential energy (CAPE) was higher than 2000 J kg^{-1} at 8:00 on 22 August (not shown). The ambient environment provided favorable conditions for deep convection formation. The duration of the storm was 23.5 h and displayed a life cycle comprising four cells (a storm is defined as a cell with CTT less than 220 K, Cell 1, Cell 2, Cell 3, and Cell 4 shown in Figure 5) that formed at 23:35 on 21 August, 23:54 on 21 August 02:52 on 22 August, and 03:41 on 22 August, respectively. Cell 3 began to merge with Cells 4 and 1 at 09:13 and 09:47, respectively, and later merged with Cell 2 at 10:22 on 22 August, producing a more intense cell. The cell traveled northward for approximately four hours before gradually weakening and was completely dissipated by 22:45.

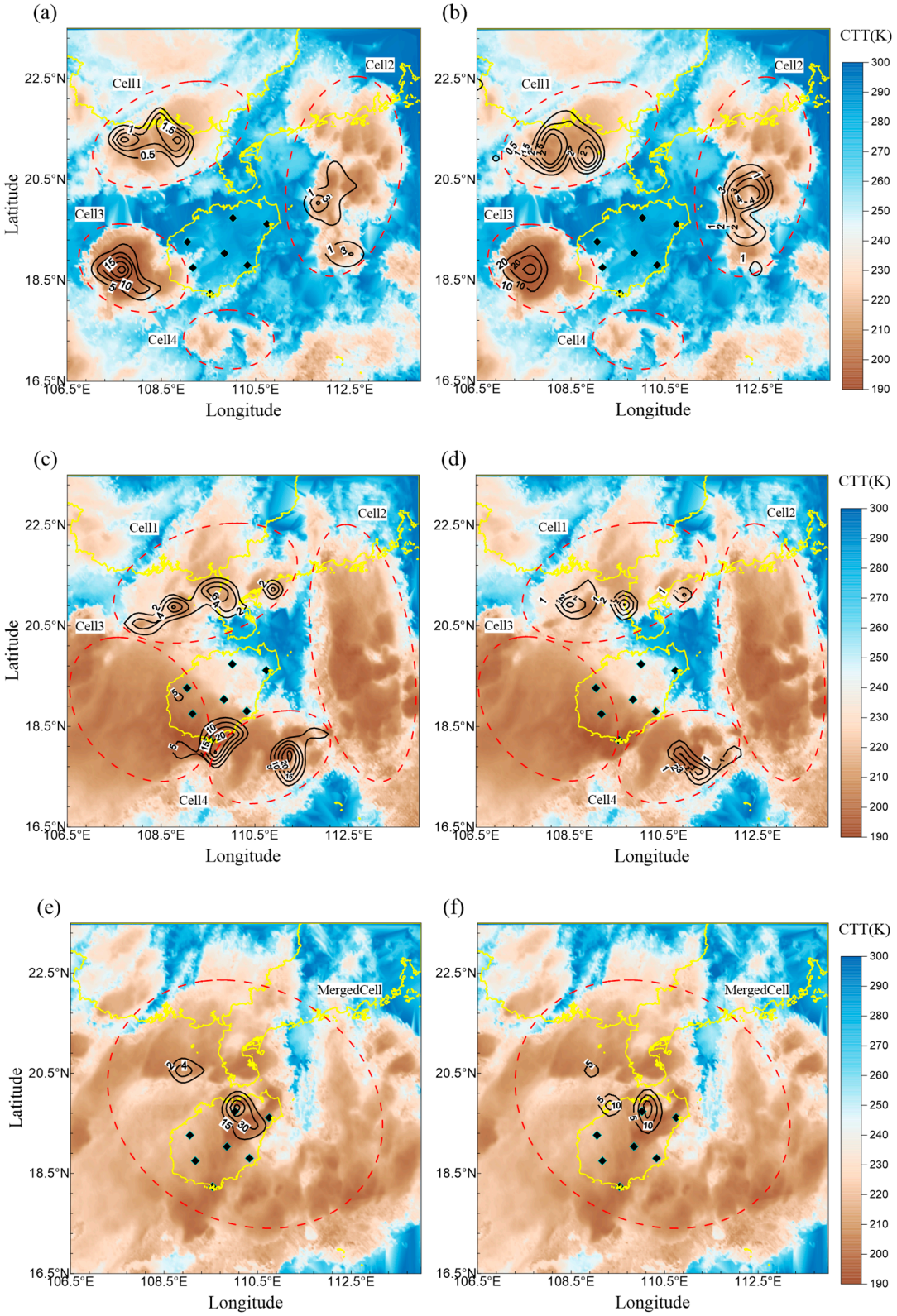

Figure 5. Cloud top temperature (CTT) during Storm0821 between (**a**,**b**) 05:00 and 05:15, (**c**,**d**) 10:00 and 10:15, and (**e**,**f**) 15:00 and 15:15 on 22 August. The black contour lines represent the density distributions (unit: $N \times 10^{-2}$ km^{-2}·h^{-1}) of the *L3D* (left panels) and lightning mapping imager group (*LMIG*, right panels) locations collected in the three periods. Solid yellow lines are the provincial borders of China; red dotted lines roughly outline the location of each cell; black diamonds represent the locations of the seven substations constituting the ground-based *L3D*.

Changes in the development of Storm0821 were visualized based on CTT data collected between 05:00 and 05:15, 10:00 and 10:15, and 15:00 and 15:15 on 22 August. In Figure 5, the colored images represent the extent of the CTT in K. Black contour lines represent the density distributions of *L3D* (left) and *LMIG* (right), the unit is 10^{-2} km^{-2}·h^{-1}. This value is used to signify the coverage and density of the lightning activities. As seen from the figure, the distributions and peak density zones of *L3D* and *LMIG* were similar. Most of the lightning is concentrated in the regions with the CTT less than 220 K, which corresponded to cells with cold tops. Before sunrise at around 05:00 on 22 August (Figure 5a,b), various cells in Storm0821 formed and gradually intensified. The peak densities of *L3D* and *LMIG* were approximately 2.7 × 10^{-1} km^{-2}·h^{-1} and 3.2 × 10^{-1} km^{-2}·h^{-1}, respectively. At about 10:00 on 22 August (Figure 5c,d), the peak densities of the *L3D* and *LMIG* were approximately 2.6 × 10^{-1} km^{-2}·h^{-1} and 3.3 × 10^{-2} km^{-2}·h^{-1}. Compared to the data collected at 05:00, the peak density of *L3D* exhibited no obvious changes, whereas that the *LMIG* data showed a drop in density, particularly for the lightning occurred after the merging of Cell 3 and Cell 4. The number of detections recorded by the *LMI* was extremely low. At around 15:00 on 22 August (Figure 5e,f), the peak densities of the *L3D* (6.3 × 10^{-1} km^{-2}·h^{-1}) was higher than that of *LMIG* (1.8 × 10^{-1} km^{-2}·h^{-1}). These results show that the two systems produced similar results in terms of coverage and density before sunrise. After the sunrise, the coverage and density of lightning detected by the *LMI* was reduced, producing a noticeable drop in the peak density of the *LMIG* compared to that of the *L3D*.

The analysis of hourly lightning activity in Storm0821 are illustrated in Figure 6. Because the observation period spans throughout a day, the black dotted lines are used to separate daytime and nighttime. The blue and red solid lines represent the hourly *L3D* pulse number (N_{L3D}) and *LMI*-group number (N_{LMIG}) in Figure 6a, respectively, whereas the black solid line represents the hourly DE_{LMI} in Figure 6b during Storm0821. The line chart shows that the number of detections increased from zero, achieved a single peak or multiple peaks, and then dropped back to zero, characterizing the formation, development, and dissipation of a thunderstorm.

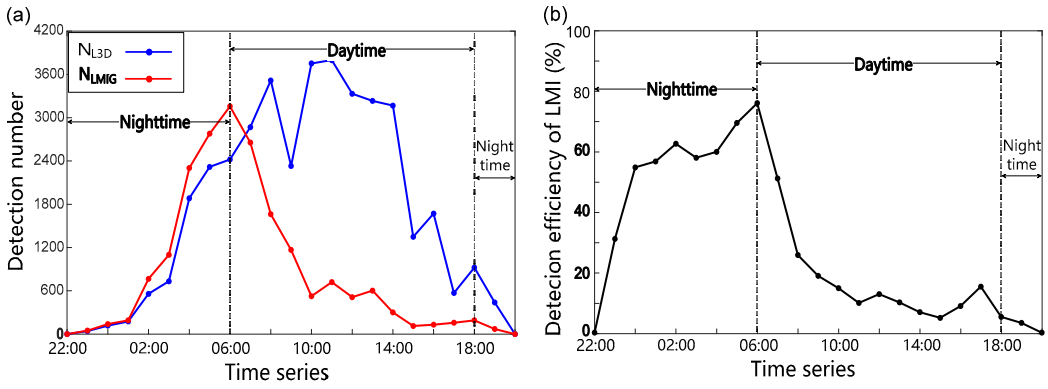

Figure 6. Hourly changes in (**a**) N_{L3D} (blue), N_{LMIG} (red) and (**b**) DE_{LMI} during the lightning activity in Storm0821. The dotted lines represent for daytime/nighttime periods during the storm.

For Storm0821, Figure 6 shows that the N_{L3D} began to rise at 01:00 on 22 August, surging from 191 to 558 within one hour. This observation suggests that the thunderstorm gradually intensified. The first peak value occurred at 08:00 on 22 August when N_{L3D} reached 3516. During this period, all of the cells were in an intense state, and the lightning activity was vigorous. The N_{L3D} reached a second peak at ~10:00, with a value of 3753. This peak was associated with the successive merging of Cell 3 with Cells 1 and 4. The intensity of the thunderstorm gradually weakened after 14:00 on 22 August, during which the N_{L3D} dropped from 3168 to 571 within three hours. Lightning activity was no longer detected at ~20:00 on 22 August, and the thunderstorm gradually dissipated. During the thunderstorm, the N_{LMIG} value grew exponentially after 01:00 on 22 August, reaching a

peak value of 3158 at around 06:00 on 22 August. Thereafter, the value dropped rapidly, reaching 526 by 10:00 on 22 August. Even though the thunderstorm reached the maximum intensity between 10:00 and 14:00 on 22 August, the N_{LMIG} value remained lower than 721 without any sign of increase. It can also be seen during the life cycle of the thunderstorm that the DE_{LMI} (Figure 6b) ranged from 31.02% to 75.93% between 23:00 on 21 August and 06:00 on 22 August, the number of *LMIG* was slightly higher than that of *L3D* in this period. After sunrise at 06:00 on 22 August, the DE_{LMI} decreased drastically from 75.93% to 14.71% within four hours. The decrease rate was 15.31% per hour.

In short, within the life cycle of Storm0821, the mean daytime DE_{LMI} was 15.46%; the mean nighttime DE_{LMI} was 50.82%, indicating a difference of 35.37% between nighttime and daytime. Distinct differences were found between daytime and nighttime detections when comparing *L3D* and *LMI*. After sunrise, the DE_{LMI} remained relatively low, even as the thunderstorms intensified. The result suggests that *LMI* performed better at night than during the daytime. Nonetheless, statistical analysis should be conducted to verify these findings.

4.2. Statistical Analysis

Besides Storm0821, 25 additional thunderstorm cases that occurred in Hainan, China, in 2019 and 2020 were used for statistical analysis. In each case, the period from the first to the last lightning pulse detected by the ground-based H-field LLSs was used which provided a comprehensive dataset for diurnal analysis. The *DE* of two LLSs within the daytime (08:00~16:00 UTC + 8) period and the night period (20:00~04:00 UTC + 8) were calculated by Bayesian theorem, and were analyzed to determine the effects of day/night factor on *LMI* performance.

The results for these cases are tabulated in Table 1. It can be seen that during the daytime, the DE_{L3D} ranged between 84.06% and 98.38%, with a mean of 92.45%, while the DE_{LMI} ranged between 2.29% and 22.65%, with a mean of 12.22%. During nighttime, the DE_{L3D} ranged between 50.84% and 83.44%, with a mean of 63.08%, while the DE_{LMI} ranged between 23.34% and 57.26%, with a mean of 43.23%. The higher DE_{L3D} in the daytime than at night was due to the assumption of P ($L3D \cup LMI$) = 1 in both day and night, results in an over estimation of DE_{L3D}, this limitation will be discussed in detail in Section 5.

Table 1. The detection ratio and *DE* of two LLSs within the daytime (08:00~16:00 UTC + 8) period and the night period (20:00~04:00 UTC + 8).

Index	Case	Daytime			Night			*DE* Diurnal Difference of *LMI*
		Detection Ratio between *LMI* and *L3D*	*DE* (%)		Detection Ratio between *LMI* and *L3D*	*DE* (%)		
			L3D	*LMI*		*L3D*	*LMI*	
1	20190816	0.15	85.09	22.65	1.26	52.50	56.08	33.42
2	20190818	0.15	84.06	21.10	1.11	50.98	56.42	35.31
3	20190819	0.15	86.32	18.60	1.09	52.09	52.75	34.15
4	20190821	0.14	91.98	15.46	0.95	55.62	50.82	35.37
5	20190827	0.06	96.87	7.53	0.63	62.91	42.01	34.48
6	20190828	\	\	\	0.62	61.30	43.96	\
7	20190829	0.07	96.07	8.06	0.87	61.28	42.75	34.69
8	20190830	0.07	94.73	11.97	0.47	70.05	37.82	25.85
9	20190905	0.12	85.27	19.21	1.18	52.16	54.73	35.52
10	20190910	\	\	\	0.51	70.85	36.88	\
11	20190915	0.07	97.23	5.12	0.41	82.53	25.99	20.87
12	20190917	0.22	90.08	12.17	0.83	61.04	40.25	28.08
13	20190925	\	\	\	1.20	50.84	57.26	\
14	20200601	0.04	97.90	7.89	\	\	\	\
15	20200604	0.11	97.18	5.49	\	\	\	\
16	20200607	0.15	90.62	15.00	0.87	51.35	50.53	35.53

Table 1. *Cont.*

Index	Case	Daytime			Night			*DE* Diurnal Difference of *LMI*
		Detection Ratio between *LMI* and *L3D*	*DE* (%)		Detection Ratio between *LMI* and *L3D*	*DE* (%)		
			L3D	*LMI*		*L3D*	*LMI*	
17	20200614	0.13	88.11	17.18	0.46	70.71	37.59	20.41
18	20200616	\	\	\	0.52	66.39	39.86	\
19	20200617	0.04	95.99	9.47	0.60	66.78	40.76	31.29
20	20200629	0.09	90.64	13.62	\	\	\	\
21	20200630	0.13	89.47	16.18	\	\	\	\
22	20200701	0.09	95.47	8.93	\	\	\	\
23	20200702	0.07	93.92	12.94	\	\	\	\
24	20200703	0.08	96.23	5.76	0.45	75.51	31.45	25.69
25	20200713	0.06	98.38	2.29	0.35	83.44	23.34	21.05
26	20200719	\	\	\	0.75	63.27	43.27	\
Mean		0.104	92.45	12.22	0.76	63.08	43.23	30.11

Combined with the detection ratio of the two LLSs, we found the detection number of *LMI* in the daytime was lower than that at night for all cases, causing the DE_{LMI} in the daytime period substantially lower than that in the night period. The day–night difference in DE_{LMI} ranged between 20.41% and 35.53%, with a mean of 30.11%. It could be concluded that day/night factor has a significant impact on the detection performance of *LMI*. Compared with the day–night difference in *DE* of LIS/OTD [6] and GLM [16], which were 12~20% and 17~29%, respectively, the influence of day/night factor on the detection performance of *LMI* was distinctly greater.

An hourly analysis was conducted and the results are shown in Figure 7. It can be seen that the DE_{LMI} rapidly dropped within about four hours after sunrise, and the DE_{LMI} rapidly increased before sunset. The sudden change in DE_{LMI} were caused by a rapid change of the detection number of *LMI* at the transition between day and night. For the storms that formed at night and lasted for an entire day, similar to Storm0821, the DE_{LMI} remained relatively low during the daytime, even as the thunderstorms intensified.

Additionally, we investigated the DE_{LMI} in different areas of the research region. As seen in Figure 8, the research region was divided into 36 subdomains, and the average DE_{LMI} of each subdomain was calculated for 26 thunderstorm cases during the day and night, respectively. During the daytime, the DE_{L3D} in the central domains ranged between 7.81% and 17.13%, with a mean of 11.75%, while the DE_{LMI} near the edges ranged between 11.41% and 19.76%, with a mean of 12.62%. During the nighttime, the DE_{L3D} in the central domains ranged between 27.55% and 52.89%, with a mean of 39.95%, and the DE_{LMI} near the edges ranged between 37.25% and 54.27%, with a mean of 41.68%. For the day–night difference in DE_{LMI}, the differences in the central domains ranged between 15.56% and 37.22%, with a mean of 28.74%, and the differences near the edges ranged between 23.73% and 38.19%, with a mean of 31.02%. As seen from the figure, there was no obvious difference in DE_{LMI} between the center of research region and the edge area whether in daytime or nighttime. The minor differences among the subdomains and the areas without any data are due to the limited sample cases, and more robust statistical results can be obtained with more measurements available in the future.

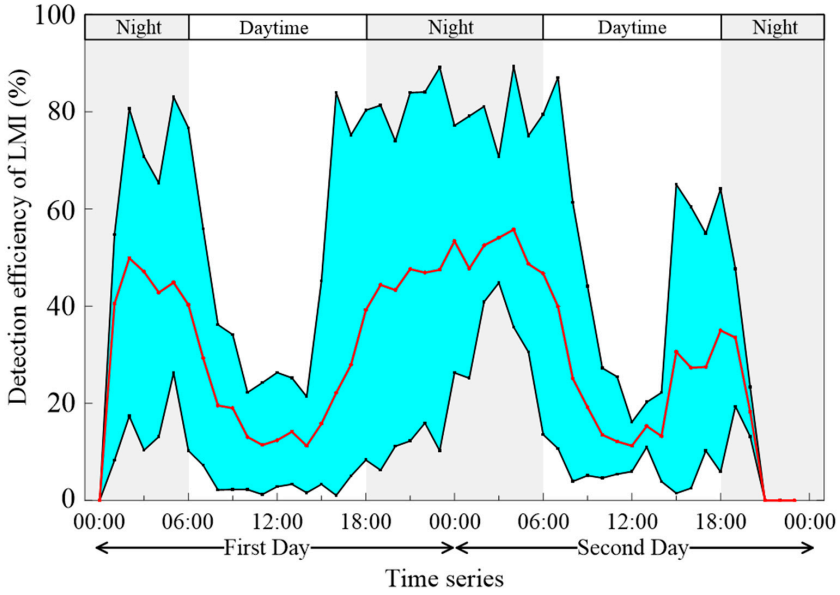

Figure 7. Hourly variation of DE_{LMI} for all the 26 thunderstorm cases. The first day is the date when a storm formed. The upper and lower boundaries of the blue shaded area are the maximum and minimum of the hourly DE_{LMI}, and the red line is the mean hourly DE_{LMI}.

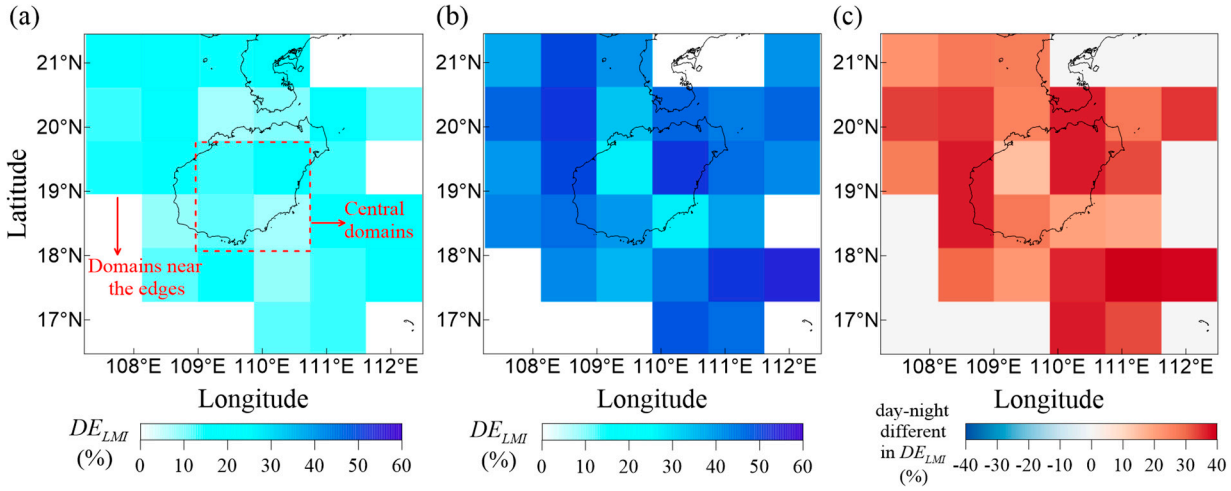

Figure 8. Spatial distribution of the average DE_{LMI} calculated based on 26 thunderstorm cases during (**a**) daytime and (**b**) nighttime, respectively. (**c**) The day-night difference in DE_{LMI}. The white images are domains indicate very few lightning detections by the two LLSs (total number less than 200).

4.3. LMI Radiative Energy Density

It can be seen from the results in Section 4.2 that the *LMI* has different *DE* for lightning activity during the daytime and night. To further understand the cause of this impact, the radiative energy density (*RED*) detected by *LMI* were used to investigate the intensity of a group. The *RED* was illustrated using the box plots for each case (Figure 9). In addition, we also counted the minimum, median, 5th and 95th percentile values of *RED* of each case, as shown in Table 2. The minimum *RED* ranged from 77.12 to 310.25 μJ sr^{-1} m^{-2} nm^{-1} and fluctuated distinctly in different cases in daytime periods, which were less than 100 μJ sr^{-1} m^{-2} nm^{-1} in 3 cases, 100~200 μJ sr^{-1} m^{-2} nm^{-1} in 9 cases, and more than 200 μJ sr^{-1} m^{-2} nm^{-1} in 9 cases. However, there was no obvious differences between the minimum *RED* for different cases at night, which was in the range of 8.38~10.63 μJ sr^{-1} m^{-2} nm^{-1}. The minimum *RED* differences between daytime and night ranged from 68.45~299.62 μJ sr^{-1} m^{-2} nm^{-1}. This suggest that the *LMI* can capture the lightning signals well with relatively

low radiation intensity (*RED* = 8.38~10.63 μJ sr^{-1} m^{-2} nm^{-1}) in the night period; however, the signals with *RED* less than 77.12 μJ sr^{-1} m^{-2} nm^{-1} cannot be detected by *LMI* in the daytime. Due to the background signal filtering (similar to GLM [28]), it can be inferred that the background noise during daytime is much higher than the noise at night because of the reflections of sunlight by clouds and atmosphere, and this may be the main reason why the group number detected by the *LMI* during daytime was much lower than that detected at night, and ultimately leads to a sharp decrease in DE_{LMI} after the sunrise. The 5th percentile *RED* ranged from 160.65 to 342.61 μJ sr^{-1} m^{-2} nm^{-1} in daytime periods and from 9.99 to 11.67 μJ sr^{-1} m^{-2} nm^{-1} at night. The median *RED* ranged from 468.84 to 1477.73 μJ sr^{-1} m^{-2} nm^{-1} in the day periods and from 24.17 to 47.50 μJ sr^{-1} m^{-2} nm^{-1} in night periods. The diurnal variation of the 5th and median percentile *RED* is the similar to the minimum values.

For some groups with extremely high intensity, the day–night difference in the 95th percentile values of DE_{LMI} was in the range of 711.60~9143.05 μJ sr^{-1} m^{-2} nm^{-1}. As seen from Figure 9, the magnitude of the extremely high *RED* in the daytime is much higher than that at night. According to the statistical analysis in Section 4.2, the DE_{LMI} at night is much higher than that at daytime, and the possibility of missing detection for high-energy groups is small. Moreover, a high-energy group with *RED* = 13,357.29 μJ sr^{-1} m^{-2} nm^{-1} was detected by *LMI* at night in Case05. It can be inferred that the groups with extreme *RED* in the daytime is the combination of the reflected sunlight and lightning activity. As the group with the *RED* exceeding 5000 μJ sr^{-1} m^{-2} nm^{-1} only accounted for 0.24% of all groups, it would not affect the results on the diurnal variation of DE_{LMI}.

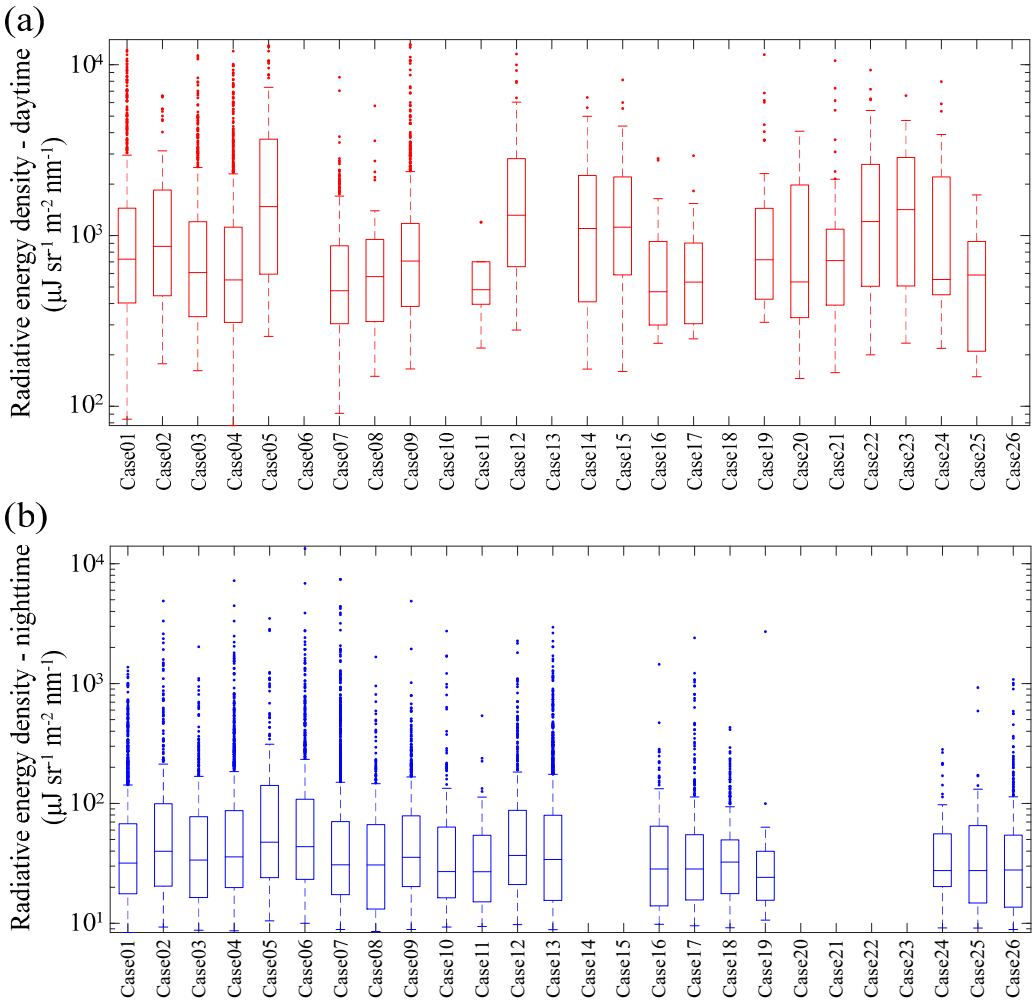

Figure 9. *RED* boxplots during (**a**) daytime and (**b**) nighttime in 26 thunderstorm cases.

Table 2. The minimum, median, 5th and 95th percentile value of radiative energy density (*RED*) in the 26 thunderstorm cases.

Index	Case	$RED_{Daytime}$ (μJ sr^{-1} m^{-2} nm^{-1})				$RED_{Nighttime}$ (μJ sr^{-1} m^{-2} nm^{-1})				$RED_{Daytime}$–$RED_{Nighttime}$(μJ sr^{-1} m^{-2} nm^{-1})			
		Min	5th	Median	95th	Min	5th	Median	95th	Min	5th	Median	95th
1	20190816	84.07	229.04	726.57	5554.27	8.38	10.36	31.76	272.84	75.69	218.68	694.82	5281.43
2	20190818	177.63	244.84	864.60	4772.22	9.32	10.95	39.85	720.69	168.31	233.89	824.75	4051.53
3	20190819	161.58	199.59	606.49	3841.92	8.75	10.18	33.67	261.78	152.83	189.41	572.82	3580.14
4	20190821	77.12	177.00	549.99	3598.11	8.67	10.53	35.81	343.38	68.45	166.47	514.19	3254.73
5	20190827	256.87	320.37	1477.73	8973.44	10.49	11.67	47.50	936.12	246.38	308.70	1430.23	8037.32
6	20190828	\	\	\	\	10.00	11.47	43.60	527.93	\	\	\	\
7	20190829	90.93	172.91	474.86	1789.65	8.87	10.68	30.74	266.62	82.06	162.23	444.12	1523.03
8	20190830	150.07	160.65	574.44	2730.94	8.54	10.41	30.64	199.62	141.46	150.24	543.80	2531.32
9	20190905	165.63	240.03	709.31	3019.41	8.88	11.00	35.47	247.01	156.75	229.03	673.84	2772.40
10	20190910	\	\	\	\	9.32	10.71	27.01	375.49	\	\	\	\
11	20190915	219.31	321.57	481.22	1195.18	9.42	10.28	26.88	109.04	209.89	311.29	454.34	1086.14
12	20190917	279.71	304.89	1314.59	6393.03	9.76	10.74	36.86	395.65	269.95	294.15	1277.74	5997.38
13	20190925	\	\	\	\	8.86	10.87	34.04	275.47	\	\	\	\
14	20200601	165.13	176.83	1099.03	4989.28	\	\	\	\	\	\	\	\
15	20200604	159.71	342.61	1118.27	4373.02	\	\	\	\	\	\	\	\
16	20200607	233.77	264.51	468.84	1644.43	9.80	10.90	28.42	198.20	223.97	253.61	440.42	1446.23
17	20200614	248.39	255.71	533.46	1537.10	9.53	10.66	28.39	179.67	238.86	245.05	505.07	1357.43
18	20200616	\	\	\	\	9.17	11.56	32.38	130.74	\	\	\	\
19	20200617	310.25	329.46	721.18	4454.33	10.63	10.88	24.17	63.29	299.62	318.58	697.02	4391.04
20	20200629	145.67	171.97	535.38	3607.83	\	\	\	\	\	\	\	\
21	20200630	157.21	182.24	712.36	5401.11	\	\	\	\	\	\	\	\
22	20200701	200.25	237.33	1206.81	5389.85	\	\	\	\	\	\	\	\
23	20200702	234.19	243.53	1418.37	4492.33	\	\	\	\	\	\	\	\
24	20200703	218.60	221.69	552.74	3792.69	9.14	9.99	27.55	210.74	209.46	211.70	525.19	3581.95
25	20200713	149.00	167.13	587.17	1301.79	9.13	10.35	27.50	131.67	139.87	156.78	559.67	1170.12
26	20200719	\	\	\	\	8.89	10.17	27.84	150.80	\	\	\	\
Mean		185.00	236.38	796.83	3945.76	9.28	10.72	32.50	299.84	178.90	229.99	677.20	3337.48

5. Discussion

5.1. Overestimation of DE Due to Assuming P (L3D∪LMI) Equals 1

In the application of the Bayesian theorem in this paper, it is assumed that all discharges could be detected by the combination of the two LLSs, i.e., *P* (*L3D∪LMI*) = 1. The *P* (*L3D∪LMI*) includes ① the pulses number detected only by *L3D*; ② he groups number detected only by *LMI*; and ③ the pulses/groups number detected by both *L3D* and *LMI*. Although *P* (*L3D∪LMI*) = 1 was assumed for both day and night periods, the total number of pulse/group *N* (*L3D∪LMI*) had a decrease affected by the poor performance of *LMI* during the daytime, and the lightning events missed by both LLSs, leading to the actual P_{day} (*L3D∪LMI*) < 1. To illustrate this issue more intuitively, we select 15 of the 26 cases that produce lightning activity in both day and night periods, the mean hourly detection number by *L3D*, *LMI* and both of them are shown in Figure 10. As seen from the figure, the lightning events missed by both LLSs is unknown, and the actual *P* (*L3D∪LMI*) is smaller than 1. According to Equations (10) and (11), a smaller numerator would result in a smaller actual *DE* than the calculated *DE*. Therefore, the *DEs* of the two LLSs were overestimated by Bayesian theorem, especially during the daytime as the *N* (*L3D∪LMI*) was lower due to the poor performance of *LMI* in the daytime.

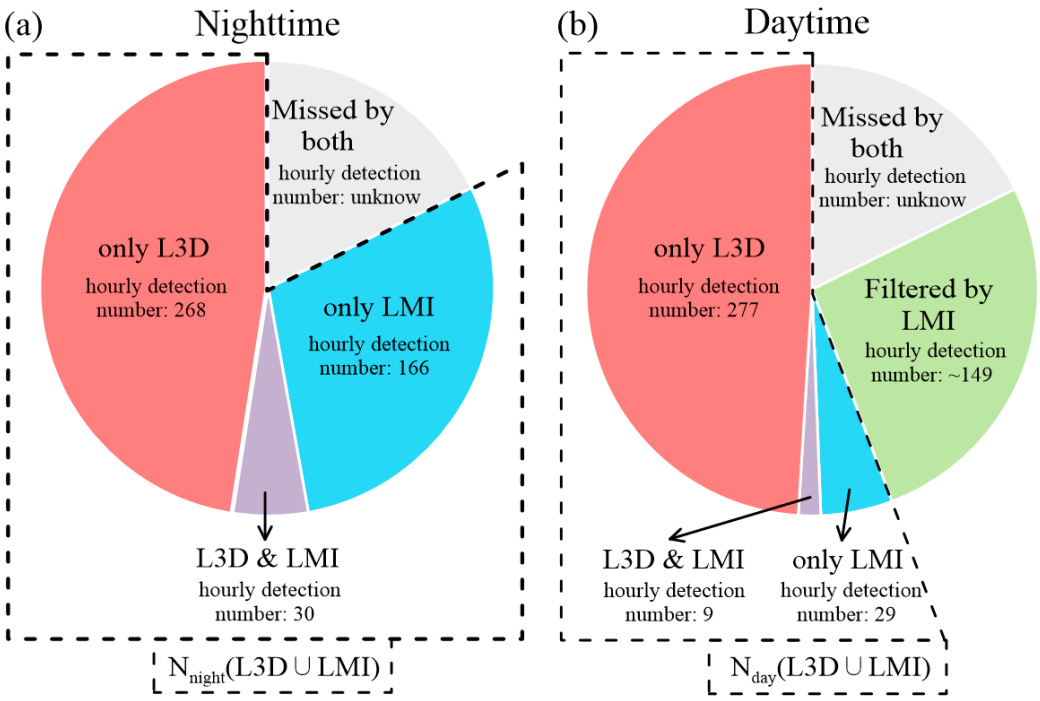

Figure 10. The hourly detection number of the two LLSs during (**a**) nighttime and (**b**) daytime. The results were derived based on the 15 thunderstorm cases spanned both day and night periods.

The ratios of the mean of hourly *N* (*L3D∪LMI*) during the night and day periods are shown in Table 3 for each case. For 80% of the cases, N_{night} (*L3D∪LMI*)/N_{day} (*L3D∪LMI*) > 1 within a range of 1.03~2.44. The remaining 3 cases with N_{night} (*L3D∪LMI*)/N_{day} (*L3D∪LMI*) < 1 was caused by that thunderstorms that developed more vigorously and *L3D* detected more pulses during the day than that at night. In addition, as seen from Figure 10, the total mean hourly N_{night} (*L3D∪LMI*)/N_{day} (*L3D∪LMI*) of the 15 cases was 1.47. Therefore, the actual day-time difference in DE_{LMI} may be larger than the range of 20.41~35.53% obtained in Section 4.2.

Table 3. The ratio of mean hourly *N* (*L3D*∪*LMI*) during night and daytime in the 15 thunderstorm cases produced lightning activity in both day and night periods.

Case	$\frac{N_{night}(L3D \cup LMI)}{N_{day}(L3D \cup LMI)}$	Case	$\frac{N_{night}(L3D \cup LMI)}{N_{day}(L3D \cup LMI)}$	Case	$\frac{N_{night}(L3D \cup LMI)}{N_{day}(L3D \cup LMI)}$
20190816	0.99	20190829	2.06	20200607	2.20
20190818	1.45	20190830	2.12	20200614	1.07
20190819	1.65	20190905	1.39	20200617	1.05
20190821	0.96	20190915	0.96	20200703	2.44
20190827	1.49	20190917	1.14	20200713	1.03

5.2. Uncertainty Due to Mismatch between the Two LLSs

For the 26 thunderstorms analyzed in this paper, the total detection number of *LMIG*s was 47,730, of which 13,991 (29.3%) groups were matched to an *L3D* pulse. For the 13,991 matches, we counted the number of *LMIG*s matched to a single *L3D* pulse. As shown in Figure 11a, 6674 (47.7%) pulses were matched to 1~3 *LMIG*s, and 4393 (31.4%) pulse were matched to 4~6 *LMIG*s. Another 2015 (14.4%) were matched to 7~9 *LMIG*s. The last 909 (6.5%) were matched to more than 9 *LMIG*s. Since the pulse from a single return stroke can be split across frames, resulting in multiple groups in one physical discharge, and the 2 s time constraint is longer than the typical duration of a discharge, there is a overestimation on *P* (*L3D* | *LMI*). The result is similar to the study by Bitzer et al. [8]. According to Equations (10) and (11), the overestimation of *P* (*L3D* | *LMI*) would result in an underestimation of DE_{LMI}, and this underestimation due to the mismatch occurred in both day and night periods. Thus, we investigated the effect of time constraint on the day–night difference in DE_{LMI}. As seen in Figure 11b, with the change of time constraints from 2.0 s to 0.5 s, the mean day–night difference in DE_{LMI} changed from 30.11% to 25.39%. However, the DE_{LMI} day–night difference is clear even for a shorter time constraint, providing confidence that the results of the strong impact of day/night factor on *LMI* are robust.

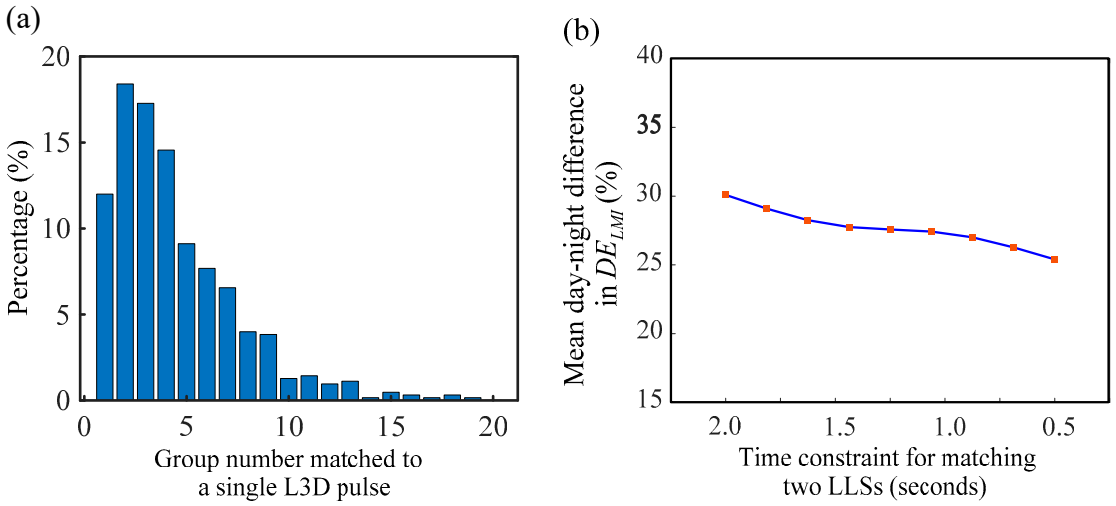

Figure 11. (**a**) The percentage of different numbers of *LMIG* matched to a single *L3D* pulse. (**b**) The change of daytime detection efficiencies of *LMI* (DELMI) day–night difference for different time constraints.

6. Conclusions

In this study, we conduct a statistical analysis using the data collected by the FY4A Lightning Mapping Imager and a ground-based low-frequency magnetic field lightning location system in the summers of 2019~2020 in Hainan, China. The effect of day/night factor on the detection performance of *LMI* was investigated by the Bayesian theorem.

The results show that for the thunderstorms in Hainan, the mean DE_{LMI} were 12.22% and 43.23% during the daytime and nighttime, respectively. The day–night difference in DE_{LMI} ranged between 20.41% and 35.53%, with a mean of 30.11%. Due to the limitations of the Bayesian theorem and the rapidly decrease of *LMI* detection number during the daytime, the actual day–night difference in DE_{LMI} was even higher than the range shown above. Compared to other space-based lightning sensors (LIS/OTD: 12~20%, GLM:17~29%), the detection performance of *LMI* was more significantly affected by the day/night factor.

The DE_{LMI} rapidly dropped within about four hours after sunrise while it increased before sunset. This phenomenon was caused by a substantial change of the *LMI* detection number at the transition between day and night. For some storms that formed at night and lasted for an entire day, the DE_{LMI} remained relatively low during the daytime, even as the thunderstorms intensified.

During night, *LMI* captured the lightning signals well with low *RED* (8.38~10.63 μJ sr^{-1} m^{-2} nm^{-1}). However, the signals with *RED* less than 77.12 μJ sr^{-1} m^{-2} nm^{-1} could not be detected by *LMI* in the daytime. It can be inferred that the background noise during daytime is far higher than the noise at night because of the reflections of sunlight by clouds and atmosphere, and this may be the main reason why the group number detected by the *LMI* during daytime was much lower than that detected at night, and ultimately leads to a significant decrease in DE_{LMI} after the sunrise.

Due to the limitations of the Bayesian theorem, the estimated *DE* in this study is "relative" *DE* rather than "absolute" *DE*. Nonetheless, the results shown in this paper clearly indicate the strong impact of day/night factor on the detection performance of *LMI*, and can be used to improve the design and post-processing method of *LMI*.

The *LMI* is the only geostationary satellite-borne lightning imager over East Asia, and can provide high temporal resolution lightning products. Understanding the effects of day/night factors on the detection performance of *LMI* provides us with a better knowledge of the application of this dataset. The findings also serve as a reference for optimizing lightning algorithms in future satellite-based lightning detection sensors.

Author Contributions: Conceptualization, H.S. and J.Y.; methodology, H.S., J.Y. and Q.Z.; software, H.S., H.G. and L.S.; formal analysis, H.S., J.Y. and X.J.; writing-original draft preparation, H.S., G.L. and K.Y.; writing-review and editing, H.S., J.Y., L.S., Q.Z., H.G., X.J., G.L. and K.Y.; supervision, J.Y. and Q.Z. All authors have read and agreed to the published version of the manuscript.

Funding: This work is supported by the National Key Research and Development Program of China (No. 2019YFC0214604), the National Natural Science Foundation of China (41905124, 42005064), the Natural Science Foundation of Jiangsu Province, China (BK20190778, BK20190777).

Acknowledgments: We thank the National Satellite Meteorological Center (NSMC) of China Meteorological Administration for providing FY4A-LMI and -AGRI datasets. We also thank the Hainan Meteorological Bureau for their help in installing the ground-based equipment and the field measurement. We appreciate the editor and three anonymous reviewers for the constructive comments and suggestions.

Conflicts of Interest: The authors declare no conflict of interest.

Abbreviations

AGRI	Advanced Geosynchronous Radiation Imager
CAPE	Convective Available Potential Energy
CCD	Charge-Coupled Device
CP	Coupled Percentage
CTT	Cloud-Top Temperature
DE	Detection Efficiency
DE_{LMI}	Detection Efficiency of Lightning Mapping Imager
ENTLN	Earth Networks Total Lightning Network
FDTD	Finite Difference Time Domain
FY4A	FengYun 4A meteorological satellite

GLM	Geostationary Lightning Mapper
GOES	Geostationary Operational Environmental Satellite
GPS	Global Position System
L3D	Low-frequency H-field Lightning Location System
LIS	Lightning Imaging Sensors
LLS	Lightning Location System
LMI	Lightning Mapping Imager
LMIG	Lightning Mapping Imager Group
NCEP	National Centers for Environmental Prediction
N_{L3D}	Number of *L3D* impulses
N_{LMI}	Number of LMI groups
OTD	Optical Transient Detectors
RED	Radiative Energy Density
RTEP	Real-Time Event Processor
TOA	Time of Arrival
VLF/LF	Very Low Frequency/Low Frequency
WGS84	World Geodetic System 1984
WWLLN	World Wide Lightning Location Network

References

1. Wolfe, W.L.; Nagler, M. Conceptual design of a space-borne lightning sensor. In Proceedings of the SPIE—The International Society for Optical Engineering, San Diego, CA, USA, 3 December 1980; Volume 246, pp. 22–33.
2. Thomson, L.W.; Krider, E.P. The Effects of Clouds on the Light Produced by Lightning. *J. Atmos. Sci.* **1982**, *39*, 2051–2065. [CrossRef]
3. Christian, H.J.; Blakeslee, R.J.; Goodman, S.J. The detection of lightning from geostationary orbit. *J. Geophys. Res. Atmos.* **1989**, *94*, 13329–13337. [CrossRef]
4. Christian, H.J.; Blakeslee, R.J.; Goodman, S.J.; Mach, D.A.; Boccippio, D.J. The Lightning Imaging Sensor. In Proceedings of the 11th International Conference on Atmospheric Electricity, Washington, DC, USA, 1 June 1999.
5. Thomas, R.J.; Krehbiel, P.R.; Rison, W.; Hamlin, T.; Boccippio, D.J.; Goodman, S.J.; Christian, H.J. Comparison of ground-based 3-dimensional lightning mapping observations with satellite-based LIS observations in Oklahoma. *Geophys. Res. Lett.* **2000**, *27*, 1703–1706. [CrossRef]
6. Boccippio, D.J.; Koshak, W.J.; Blakeslee, R.J. Performance Assessment of the Optical Transient Detector and Lightning Imaging Sensor. Part I: Predicted Diurnal Variability. *J. Atmos. Ocean. Technol.* **2002**, *19*, 1318–1332. [CrossRef]
7. Thompson, K.B.; Bateman, M.G.; Carey, L.D. A Comparison of Two Ground-Based Lightning Detection Networks against the Satellite-Based Lightning Imaging Sensor (LIS). *J. Atmos. Ocean. Technol.* **2014**, *31*, 2191–2205. [CrossRef]
8. Bitzer, P.M.; Burchfield, J.C.; Christian, H.J. A Bayesian Approach to Assess the Performance of Lightning Detection Systems. *J. Atmos. Ocean. Technol.* **2016**, *33*, 563–578. [CrossRef]
9. Goodman, S.J.; Blakeslee, R.J.; Koshak, W.J.; Mach, D.; Bailey, J.; Buechler, D.; Carey, L.; Schultz, C.; Bateman, M.; McCaul, E.; et al. The GOES-R Geostationary Lightning Mapper (GLM). *Atmos. Res.* **2013**, *125-126*, 34–49. [CrossRef]
10. Rudlosky, S.D.; Goodman, S.J.; Koshak, W.J.; Blakeslee, R.J.; Buechler, D.E.; Mach, D.M.; Bateman, M. Characterizing the GOES-R (GOES-16) Geostationary Lightning Mapper (GLM) on-orbit performance. In Proceedings of the 2017 IEEE International Geoscience and Remote Sensing Symposium, Fort Worth, TX, USA, 23 July 2017; pp. 279–282. [CrossRef]
11. Rudlosky, S.D.; Goodman, S.J.; Virts, K.S.; Bruning, E.C. Initial Geostationary Lightning Mapper Observations. *Geophys. Res. Lett.* **2019**, *46*, 1097–1104. [CrossRef]
12. Yang, J.; Zhang, Z.; Wei, C.; Lu, F.; Guo, Q. Introducing the New Generation of Chinese Geostationary Weather Satellites, Fengyun-4. *Bull. Am. Meteorol. Soc.* **2017**, *98*, 1637–1658. [CrossRef]
13. Liu, R.; Liu, T.; Pessi, A.; Hui, W.; Cheng, W.; Huang, F. Preliminary study on the influence of FY-4 lightning data assimilation on precipitation predictions. *J. Trop. Meteorol.* **2019**, *25*, 528–541. (In Chinese)
14. Chan, Y.W.; So, C.K. The applications of Feng Yun 4 A satellite products for weather monitoring over the asian regions. In Proceedings of the 99th American Meteorological Society Annual Meeting, Phoenix, AZ, USA, 10 January 2019.
15. Peterson, M. Research Applications for the Geostationary Lightning Mapper Operational Lightning Flash Data Product. *J. Geophys. Res. Atmos.* **2019**, *124*, 10205–10231. [CrossRef]
16. Marchand, M.; Hilburn, K.; Miller, S.D. Geostationary Lightning Mapper and Earth Networks Lightning Detection Over the Contiguous United States and Dependence on Flash Characteristics. *J. Geophys. Res. Atmos.* **2019**, *124*, 11552–11567. [CrossRef]
17. Zhang, D. Inter-Comparison of Space-and Ground-Based Observations of Lightning. Ph.D. Thesis, University of Arizona, Tucson, AZ, USA, 2019.
18. Zhang, D.; Cummins, K.L. Time Evolution of Satellite-Based Optical Properties in Lightning Flashes, and its Impact on GLM Flash Detection. *J. Geophys. Res. Atmos.* **2020**, *125*. [CrossRef]

19. Rutledge, S.A.; Hilburn, K.A.; Clayton, A.; Fuchs, B.; Miller, S.D. Evaluating Geostationary Lightning Mapper Flash Rates within Intense Convective Storms. *J. Geophys. Res. Atmos.* **2020**, *125*. [CrossRef]
20. Hui, W.; Zhang, W.; Lyu, W.; Li, P. Preliminary Observations from the China Fengyun-4A Lightning Mapping Imager and Its Optical Radiation Characteristics. *Remote Sens.* **2020**, *12*, 2622. [CrossRef]
21. Liu, R.X.; Lu, Q.F.; Min, C.; Zhang, Y.; Li, X.Q. Quality Assessment of FY-4A Lightning Data in Inland China. *J. Trop. Meteorol.* **2020**, *26*, 286–299.
22. Jing, X.; Geerts, B.; Wang, Y.; Liu, C. Evaluating Seasonal Orographic Precipitation in the Interior Western United States Using Gauge Data, Gridded Precipitation Estimates, and a Regional Climate Simulation. *J. Hydrometeorol.* **2017**, *18*, 2541–2558. [CrossRef]
23. Lyu, F.; Cummer, S.A.; Solanki, R.; Weinert, J.; McTague, L.; Katko, A.; Barrett, J.; Zigoneanu, L.; Xie, Y.; Wang, W. A low-frequency near-field interferometric-TOA 3-D Lightning Mapping Array. *Geophys. Res. Lett.* **2014**, *41*, 7777–7784. [CrossRef]
24. Lyu, F.; Cummer, S.A.; Lu, G.; Zhou, X.; Weinert, J. Imaging lightning intracloud initial stepped leaders by low-frequency interferometric lightning mapping array. *Geophys. Res. Lett.* **2016**, *43*, 5516–5523. [CrossRef]
25. Yoshida, S.; Wu, T.; Ushio, T.; Kusunoki, K.; Nakamura, Y. Initial results of LF sensor network for lightning observation and characteristics of lightning emission in LF band. *J. Geophys. Res. Atmos.* **2014**, *119*, 12034–12051. [CrossRef]
26. Zhang, X.H. 3-D Lightning Location Based on Low Frequency Magnetic Field and Preliminary Detection Performance Assessment of Lightning Mapping Imager on FY-4A Geostationary Meteorological Satellite. Master's Thesis, Nanjing University of Information Science & Technology, Nanjing, China, 2019. (In Chinese)
27. Liu, C. Development and Application of Multi-Gain Lightning Electromagnetic Pulse Sensor. Master's Thesis, Nanjing University of Information Science & Technology, Nanjing, China, 2019. (In Chinese)
28. Mach, D.M.; Bateman, M.G.; Blakeslee, R.J.; Boldi, R.A.; Buechler, D.E.; Carey, L.D.; Goodman, S.J.; Koshak, W.J.; McCaul, E.W.; Peterson, W.A. GOESR Geostationary Lightning Mapper performance specifications and algorithms. In Proceedings of the 2008 NOAA STAR GOES-R AWG Review, Madison, WI, USA, 24 August 2008.
29. Boccippio, D.J.; Driscoll, K.; Hall, J.; Buechler, D. *LIS/OTD Software Guide*; Technical Report; NASA: Washington, DC, USA, 1998.
30. Ushio, T.; Driscoll, K.; Heckman, S.; Boccippio, D.; Koshak, W.; Christian, H. Initial comparison of the Lightning Imaging Sensor (LIS) with Lightning Detection and Ranging (LDAR). In Proceedings of the 11th International Conference on Atmospheric Electricity, Washington, DC, USA, 1 June 1999.
31. Mach, D.M.; Christian, H.J.; Blakeslee, R.J.; Boccippio, D.J.; Goodman, S.J.; Boeck, W.L. Performance assessment of the Optical Transient Detector and Lightning Imaging Sensor. *J. Geophys. Res. Atmos.* **2007**, *112*. [CrossRef]
32. Min, M.; Chunqiang, W.; Chuan, L.; Hui, L.; Na, X.; Xiao, W.; Lin, C.; Fu, W. Developing the science product algorithm testbed for Chinese next-generation geostationary meteorological satellites: Fengyun-4 series. *J. Meteorol. Res.* **2017**, *31*, 708–719. [CrossRef]
33. Zhang, P.; Zhu, L.; Tang, S.; Gao, L.; Chen, L.; Zheng, W.; Han, X.; Chen, J.; Shao, J. General Comparison of FY-4A/AGRI with Other GEO/LEO Instruments and Its Potential and Challenges in Non-meteorological Applications. *Front. Earth Sci.* **2019**, *6*, 224. [CrossRef]
34. Yang, J.; Wang, Z.; Heymsfield, A.J.; DeMott, P.J.; Twohy, C.H.; Suski, K.J.; Toohey, D.W. High Ice Concentration Observed in Tropical Maritime Stratiform Mixed-Phase Clouds with Top Temperatures Warmer than −8 °C. *Atmos. Res.* **2020**, *233*, 104719. [CrossRef]